Chapter 13

Field-Induced Nanoscale Water Bridges and Tip-Based Oxidation Nanolithography

Ricardo Garcia
Instituto de Microelectronica de Madrid, CSIC, 28760 Tres Cantos, Spain
ricardo.garcia@imm.cnm.csic.es

What once was considered a nuisance in surface science, the spontaneous adsorption of water on surfaces, is now a key element to develop some nanolithographies based on the spatial confinement of chemical and/or electrochemical reactions within the limits of a nanoscale meniscus. In this chapter, I introduce some of the fundamental aspects of the field-induced formation of water and other liquid bridges between two solid surfaces. The role of the different energy contributions such as the condensation, surface, van der Waals, and electrostatic energies are discussed. Special attention is devoted to describe the formation of field-induced nanoscale liquid bridges in a force microscope interface. The last section of the chapter is devoted to introducing tip-based oxidation nanolithography. There, the control and manipulation of water bridges has enabled the fabrication of sophisticated electronic and

Nanoscale Liquid Interfaces: Wetting, Patterning, and Force Microscopy at the Molecular Scale
Edited by Thierry Ondarçuhu and Jean-Pierre Aimé

ISBN 978-981-4316-45-3 (Hardcover), 978-981-4364-48-5 (eBook)
www.panstanford.com

mechanical nanodevices, as well as the construction of molecular architectures.

13.1 Introduction

Water adsorbs spontaneously on surfaces. The thickness of the wetting layer is controlled by the relative humidity, the temperature, and the surface energies.[1–6] When two surfaces are brought together, the above phenomenon could lead to the formation of a water bridge between the surfaces. The bridge, in equilibrium with the vapor, forms a concave meniscus of a negative mean curvature defined by the Kelvin equation.[1–4,7–8] This equation is valid for systems down to menisci of radius of 3 nm.[7–9] The formation of wetting layers and small capillaries are issues of great scientific and technological interest because they are present in a wide range of phenomena such as friction, lubrication, dissipation, dispensing, nanofabrication, and high-resolution imaging.[10–23] In particular, atomic force microscopy (AFM) imaging in air could be largely affected by the formation of a water meniscus.[22–29] The capillary force could increase the net force exerted on the substrate. This, in turn, could imply its modification and/or a deterioration of the spatial resolution. Evidence of the meniscus formation can be inferred by taking force versus distance curves. The presence of a large hysteresis curve is indicative of the meniscus formation[22–23,28] In fact, the minimization of the lateral force between the tip and the sample to avoid the formation of a stable water meniscus was one of the motivations to develop amplitude modulation AFM.[29–31]

However, the presence of a water bridge turns out to be very useful to perform local electrochemical processes or to control the deposition of molecules, and thus novel lithography and patterning methods have been proposed[19–21,32–40] (see also chapter 12). In particular, AFM (tip-based) oxidation nanolithography has emerged as a highly reliable patterning method.[19,41–58] Tip-based oxidation experiments are performed by applying an external voltage. As a consequence, the external voltage has a dual role. On the one hand, it induces the formation of the liquid meniscus, and on the other hand, it activates the electrochemical process.

The chapter is divided into two sections. In the first section, the main factors that participate in the formation of a nanoscale water bridge in the presence of an electric field are described. In the second section, I introduce some examples of the use of water bridges for patterning and fabricating nanolectronic devices.

13.2 Field-Induced Formation of a Nanoscale Water Bridge

13.2.1 *Spontaneous Formation of a Water Meniscus: Kelvin Equation*

In ambient conditions water spontaneously condenses from vapor into the cavities of hydrophilic surfaces. Water condensation is a thermodynamic process that links the vapor pressure of a liquid with its curvature in the condensed form. It is described by the Kelvin equation,[1−4,7−9]

$$R_{\mathrm{g}}T \ln \frac{p}{p_0} = \frac{\gamma_{\mathrm{L}} \nu_{\mathrm{m}}}{r_{\mathrm{K}}} \tag{13.1}$$

where the Kelvin radius r_{K} gives information on the size of the meniscus,

$$\frac{1}{r_K} = \frac{1}{r_1} + \frac{1}{r_2} \tag{13.2}$$

where R_{g} is the gas constant, γ_{L} is the surface tension of liquid, p is the actual vapor pressure, p_0 is the vapor pressure at saturation, ν_{m} is the molar volume of the liquid, and r_1 ($r_1 < 0$) and r_2 ($r_2 > 0$) are the principal radii of curvature of the meniscus (Fig. 13.1). In the case of water condensation, p/p_0 is the relative humidity. The Kelvin equation states that in equilibrium the size of the capillary where condensation occurs is determined by the vapor pressure. As a consequence, condensation occurs at a relative humidity below 100% for curved surfaces. In an AFM interface a water meniscus could be formed whenever the tip and the sample gap distance is equal or smaller than the Kelvin radius. For example, at ambient conditions ($p/p_0 = 0.5$ or 50% relative humidity and $T = 293$ K with nm), Eq. 13.1 gives a Kelvin radius of -0.78 nm, which indicates that pores or cavities of sizes below 2 nm should be filled with water.

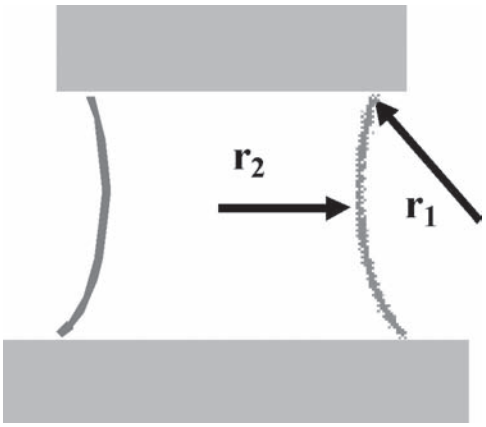

Figure 13.1 Model of the geometry of a water meniscus bridging two flat surfaces. The main curvature radii are indicated.

13.2.2 *Water Bridge Formation Induced by an Electric Field*

At ambient conditions the formation of a water bridge between two surfaces requires very small separations. For gap distances above 3 nm, the formation of a water bridge requires the participation of an additional force such as the one provided by an electric field. The process of forming a water bridge is a dynamic one, where water molecules condense and evaporate at the same time. In the absence of an electric field, the times needed to reach the equilibrium configuration for a capillary condensate vary with its size.[59–61] For example, formation times of 5 ms have been reported for a water meniscus with a curvature radius in the sub-10 nm range.[13,61]

Some aspects of the formation of capillaries under the presence of an electric field are often studied in electrowetting.[62–66] There are a significant number of simulations at the continuum level to describe the field-induced formation of liquid bridges.[67–73] The understanding of the elemental aspects of a water bridge formation is simplified by examining the different contributions to the total energy of the system. The energy involved in the formation of a nanoscale liquid bridge in the presence of an electric field has contributions from surface U_s, condensation U_c, van der Waals U_{vdW}, and electrostatic U_e energies. The different contributions to the

energy are calculated by the following expressions:[69,73–74]

$$U_{\mathrm{s}} = \gamma \int_S \mathrm{d}\vec{s} \tag{13.3}$$

where γ is the surface energy of the relevant interface (liquid–vapor, liquid–solid, or solid–vapor), in a first approximation[4] $\gamma \approx \gamma_{\mathrm{LV}} \approx \gamma_{\mathrm{SV}} - \gamma_{\mathrm{LS}}$, where $\gamma_{\mathrm{LV}}, \gamma_{\mathrm{SV}}$, and γ_{LS} are, respectively, the energies per unit surface of the liquid-vapor, solid-vapor, and liquid-solid surfaces.

$$U_{\mathrm{c}} = \frac{R_{\mathrm{g}} T}{v_{\mathrm{m}}} \ln\left(\frac{1}{RH}\right) \int_V \mathrm{d}\vec{r} \tag{13.4}$$

where v_{m} is the molar volume and $R_{\mathrm{g}} = 8.31\ \mathrm{Jmol^{-1}K^{-1}}$ the gas constant. The condensation energy is proportional to the volume of the liquid and the temperature T. It also depends logarithmically on the ratio p/p_0, which for water is identified with the relative humidity RH expressed in percentage values. The electrostatic energy associated with the polarization of the water induced by the electric field is calculated by

$$U_{\mathrm{e}} = \frac{\varepsilon 0}{2} \int_V \varepsilon E^2 \mathrm{d}\vec{r} \tag{13.5}$$

where E is the electric field just before water condensation, ε_0 the dielectric constant of the air, and ε the relativity dielectric constant of the liquid. The energy associated with the van der Waals forces between water molecules is given by

$$U_{\mathrm{vdW}} = \frac{H}{12\pi} \int_S \frac{1}{\xi^2} d\vec{s} \tag{13.6}$$

where H is the Hamaker constant and ξ is a function that depends on the shape of the liquid and can be approximated to the distance between the bottom and top layers of the liquid. Given the relatively short-range character of van der Waals forces, this contribution only becomes important for very small separations (1–4 nm).

The formation of a stable water bridge requires a decrease in the energy of the condensed state with respect to the noncondensed state U_0, that is, the sign of Eq. 13.7 for a given electric field, relative humidity, and temperature has to be negative.

$$\Delta U = U(\text{bridge}) - U_0(\text{vapor}) = \Delta U_{\mathrm{s}} + \Delta U_{\mathrm{c}} + \Delta U_{\mathrm{vsW}} + \Delta U_{\mathrm{e}} \tag{13.7}$$

In Eq. 13.7, U_e and U_c are the larger contributions; however, U_s and U_{vdW} have a pivotal role to determine the surface profile of the water in the condensed configuration.

13.2.3 *Field-Induced Water Bridge Formation between Two Parallel Metallic Plates*

To provide a realistic description of the steps involved in the formation of a nanoscale water bridge requires determining the shape of the water protrusion induced by the field. This is a nonlocal problem that requires, among other things, determining the electric field for the relevant interface geometry, in particular the tip–surface interface. However, insight into the physical parameters that influence the formation of a water bridge for a curved surface can be gained by studying the formation of a water bridge between two parallel and conducting surfaces under the application of a voltage V.[69] For a parallel geometry the polarity of the voltage does not have any influence on the process.

The energy required to condense a cylindrical liquid column of diameter W, bridging the gap D between the metallic surfaces (Fig. 13.2), is the sum of the surface, condensation, van der Waals, and electrostatic contributions. From Eq. 13.3 it can be deduced that the surface energy change involve in the condensation of a

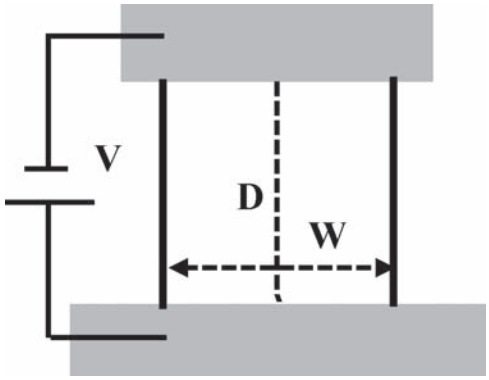

Figure 13.2 Scheme of the interface for a cylindrical liquid column formed between two flat surfaces in the presence of an applied voltage.

cylindrical water bridge is given by

$$\Delta U_{\mathrm{s}} = \pi W D \gamma_{LV} - \pi \frac{W^2}{2}(\gamma_{SV} - \gamma_{LS}). \tag{13.8}$$

On the other hand, at temperature T, the condensation energy from the vapor phase is proportional to the bridge volume:

$$\Delta U_{\mathrm{c}} = \frac{R_{\mathrm{g}} T}{v_{\mathrm{m}}} \ln\left(\frac{1}{RH}\right) \frac{\pi W^2 D}{4} \tag{13.9}$$

In the presence of a voltage, the electrostatic energy ΔU_{e} associated with the polarization of the condensed liquid is given by

$$\Delta U_{\mathrm{s}} = \pi W D \gamma_{LV} - \frac{\pi W^2}{2}(\gamma_{SV} - \gamma_{LS}), \tag{13.10}$$

while the energy associated to the van der Waals forces is given by

$$\Delta U_{\mathrm{vdW}} = \frac{H}{12\pi} \int_S \frac{r}{r^2} dr = \frac{h_0}{2}\left(\frac{h_0^2}{D^2} - 1\right) \frac{R_g T}{v_m} \ln\left(\frac{1}{RH}\right) \tag{13.11}$$

$$h_0^3 = \frac{|A|}{6\pi}\left[\frac{RT}{v_m} \ln\left(\frac{1}{RH}\right)\right]^{-1} \tag{13.12}$$

where h_0 is the thickness of the wetting layer on the surface in the absence of an applied voltage. Here, the change of the van der Waals energy is calculated between two configurations, the water bridge and a thin film of water adsorbed on the bottom surface. Then, the total energy change due to the condensation of water is given by

$$\Delta U \approx \frac{\pi W^2 D}{4}\left[\frac{R_{\mathrm{g}} T}{v_{\mathrm{m}}} \ln\left(\frac{1}{RH}\right) - \frac{2\gamma}{D} - \frac{1}{2D^2}(\varepsilon - 1)\varepsilon_0 V^2\right] + \pi \gamma W D - \frac{h_0}{2}\frac{R_{\mathrm{g}} T}{v_{\mathrm{m}}} \ln\left(\frac{1}{RH}\right). \tag{13.13}$$

In general, the formation of a water bridge is favored by the electrostatic and van der Waals energies and opposed by the surface and condensation energies. Remarkably, the above expression shows that for any separation between the plates, D, there is a threshold voltage that corresponds to the liquid filling the gap between the plates. An expression of the threshold voltage is obtained by neglecting the thickness of the water layer at zero field ($h_0 \approx 0$), which could be 1–3 water molecules in thickness, and then[69]

$$V_{\mathrm{th}} \approx \frac{2D}{\varepsilon_0(\varepsilon - 1)}\left[D \frac{R_{\mathrm{g}} T}{v_{\mathrm{m}}} \ln\left(\frac{1}{RH}\right) - 2\gamma\right]. \tag{13.14}$$

13.2.4 *Field-Induced Water Bridge Formation in a Nonplanar Interface*

Numerical simulations that include the geometry for a nonplanar interface as well as the shape of the water protrusion give a more detailed picture of the different regimes involved in the formation of a field-induced nanoscale water bridge.[69,72–74]

Figure 13.3 shows a model to describe an interface characterized by a parabolic tip and a flat surface. In this model, the droplet is described by a hyperbolic function that has radial symmetry ρ, and it is parameterized by the height at its maximum h and the width at half-maximum w. The surface profile of the droplet is described by[73]

$$z(\rho) = h_0 + \frac{h}{\cosh(\rho/w)}. \tag{13.15}$$

The electric field generated by applying a voltage V is approximated by the one produced by a sphere of radius R. Furthermore, the field has a radial symmetry, as shown in Fig. 13.3, and is calculated by using a spherical capacitor with the tip placed at its center.[69] The above geometry has special relevance because it contains the main elements that characterize an AFM interface. The simulations show the existence of three main regimes.[73] Two of them are

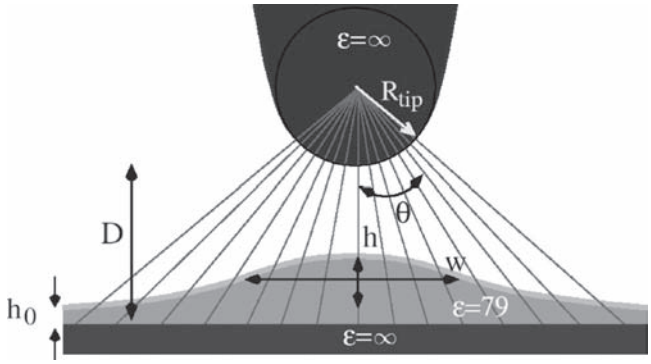

Figure 13.3 Model for simulating the formation of a nanoscale water bridge under an electric field. The field is calculated by assuming a radial distribution; h_0 is the thickness of the adsorbed water layer in the absence of an electric field; h is the maximum height of the droplet induced by the field (total droplet height $= h_0 + h$); and w is width of the liquid protrusion induced by the field at half height.

characterized by the existence of a single and stable configuration, while the other shows the coexistence of two stable configurations or geometries for the water condensate.

Figure 13.4 shows the minimum of the energy ΔU as a function of the height of the protrusion formed in the vicinity of the tip apex for several applied voltages. For low voltages, the interface is characterized by a single stable water shape. The total energy

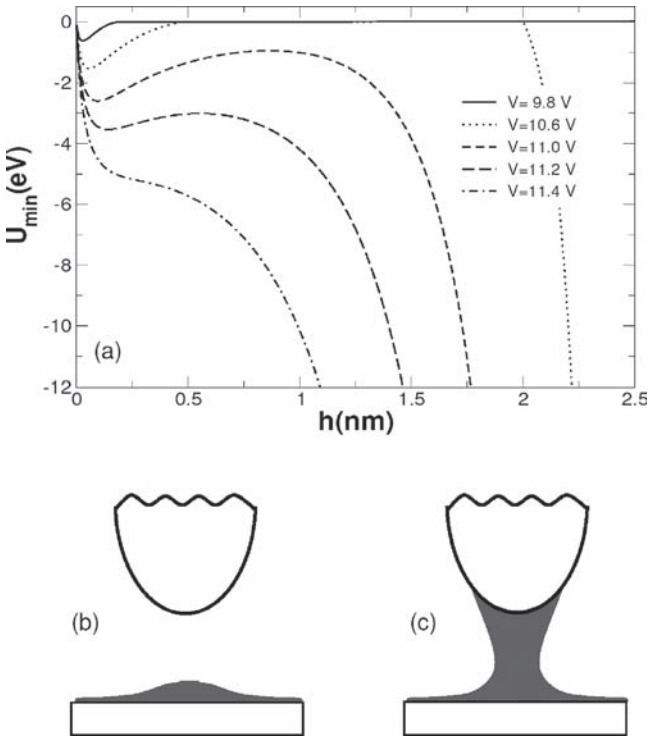

Figure 13.4 Potential energy curves for several voltages as a function of the height of the water droplet. For low voltages, the energy curve shows a minimum very close to the sample surface. Above a certain critical voltage, the curve shows two minima, a local minimum close to the surface and an absolute minimum where the liquid fills the gap. The calculations are performed for a gap distance of 6 nm and $RH = 37\%$. Schematic representation of the two stable configurations associated with, respectively, (b) the first local minimum (droplet) and (c) the liquid bridge. (Data adapted from Ref. 73.)

has a minimum very close to the sample surface (Fig. 13.4a). This minimum corresponds to the formation of a very small protrusion of the water film (droplet) underneath the strongest field lines. The total thickness of the protrusion is $z = h_0 + h$. For voltages above 11.3 V ($D = 6$ nm, and $R_t = 30$ nm), it is not possible to find a droplet geometry that minimizes the energy. The droplet becomes unstable, and a liquid meniscus bridges the gap between tip and surface. However, there is a range of intermediate voltages ($\approx$11–11.2 V) where the energy has two minima with respect to h. The existence of two minima implies the coexistence of two stable water shapes. The local minimum close to the surface is associated with the formation of a droplet under the tip apex (Fig. 13.4b), while the absolute minimum is associated with a configuration where the liquid fills the tip–surface gap (Fig. 13.4c). By increasing the voltage, the local minimum decreases and eventually disappears. The droplet becomes unstable, and the only stable condensate is the water bridge.

The existence of single and bimodal regimes implies the existence of two characteristic voltages and a hysteresis behavior. The lower voltage V_{m} is defined as the minimum voltage that sustains a liquid bridge. It marks the transition from a single configuration (droplet) to a bimodal configuration (droplet and water bridge). This voltage depends on the relative humidity, temperature, and tip–surface geometry. At higher voltages, another characteristic voltage is found. This voltage is called the threshold voltage V_{th}. It defines the transition from the coexistence of the droplet and the water bridge condensates to a single configuration characterized by the water bridge.

The coexistence of two water shapes for some voltages and distances and the activation barrier that separates them introduces a history-dependent behavior or hysteresis. For example, if a voltage sequence is applied from low to high voltages, the most favorable configuration is the formation of a water protrusion under the tip. When the voltage is above the threshold value, the droplet collapses and a water bridge is formed. However, once the liquid bridge has been formed, the voltage could be lowered to an intermediate range of values between V_{m} and V_{th} without evaporating the bridge.

The above discussion has been focused on describing the field-induced formation of water bridges; however, the same equations and methodology can be used to describe the formation of other liquid bridges. The only requirement is to use the values of the dielectric constant, the surface energy, the molar volume, and the Hamaker constant that characterize the liquid.

Figure 13.5 shows the comparison between theory and experiment for the formation of water and ethanol nanoscale liquid bridges. The dependence of the threshold voltage as a function of the average tip–surface separation shows a remarkable agreement between the measured and calculated V_{th} values for the formation of water and ethanol water bridges. The threshold voltage increases monotonically with the average tip–surface separation in both cases. For the same tip–surface separation, the formation of nanoscale water bridges requires slightly higher voltages because the condensation energy for water is higher—$\text{v}_{\text{m}}(\text{water}) < \text{v}_{\text{m}}(\text{ethanol})$. Furthermore, the comparison of surface energies ($\gamma_{\text{eth}} < \gamma_{\text{water}}$) also favors, for the same conditions, the formation of ethanol protrusions. Those effects offset the influence of the dielectric constant in the electrostatic energy ($\varepsilon_{\text{water}} > \varepsilon_{\text{eth}}$).

The electric fields associated with the formation of a water bridge in a force microscope interface are extremely high ($\approx 1\ \text{V nm}^{-1} = 10^9\ \text{V/m}$). The electric field at the solid–liquid interface for a droplet just before the formation of a water bridge is about one to two orders of magnitude smaller than the one inside the bridge. The dependence of the maximum electric field at the silicon interface is depicted in the insets of Fig. 13.5. Two fields are calculated, the electric field at the solid–liquid interface underneath the tip's axis for a bias just below V_{th} (solid line) and the field for a voltage just above V_{th} (discontinuous line).

13.2.5 *Field-Induced Water Bridge Formation: Molecular Dynamics Simulations*

Information at the molecular level of the changes experienced by the water molecules in the presence of a field is provided by molecular dynamics simulations.[74] For a water drop deposited on a solid surface (droplet), the dipole moments of the molecules situated

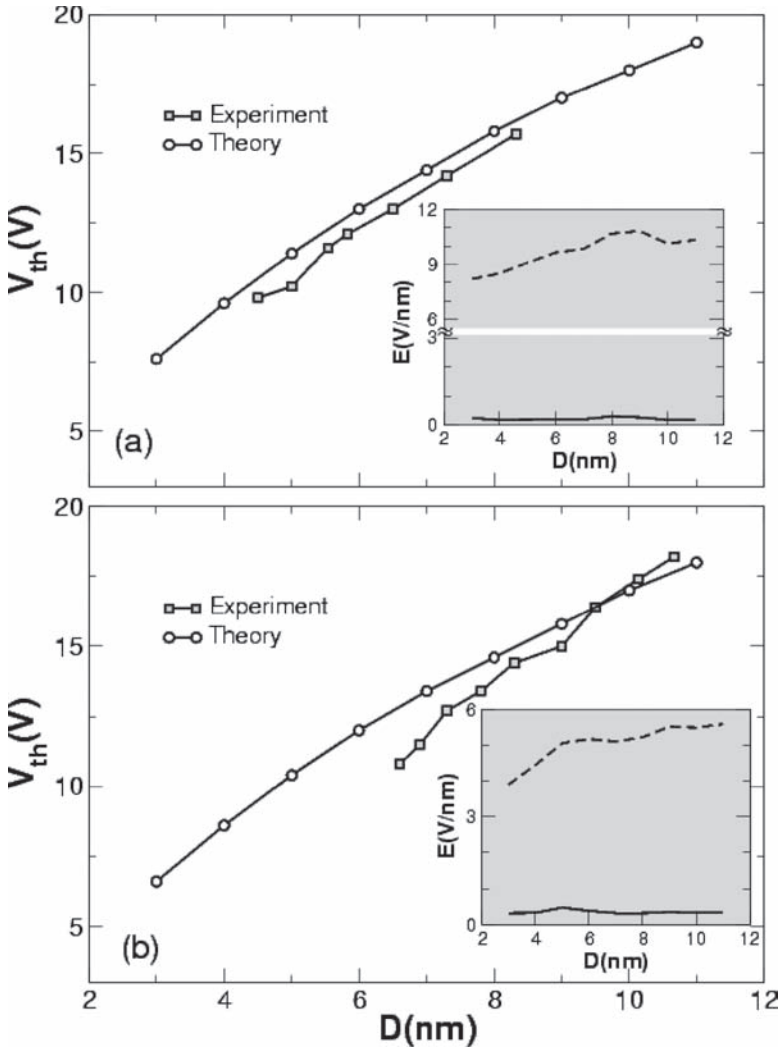

Figure 13.5 Threshold voltage dependence on the tip–surface separation. (a) Water, $RH = 30\%$. (b) Ethanol. The inset shows the dependence of the maximum electric field on the tip–surface separation just before (solid line) and after (dotted line) the liquid bridge formation. The model uses a tip radius of 30 nm. (Data adapted from Ref. 73.)

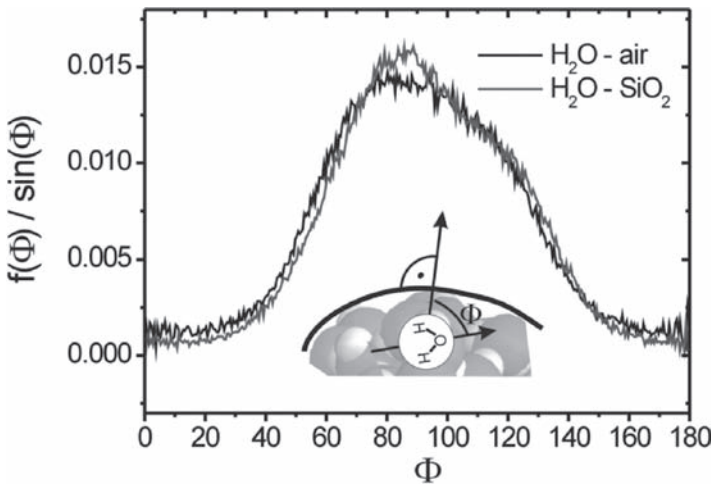

Figure 13.6 Molecular dynamics simulations of the orientation of water molecules. Alignment of the water molecules at the air–drop and silicon dioxide–drop interfaces at 0 V: gray for the silicon dioxide surface and black for the air interface. The angle Φ is between the dipole moment of a water molecule and the normal to the surface. The distribution is normalized by sin(Φ) to give the statistical probability. (Data adapted from Ref. 74.)

at the water–air and water–solid interfaces are not randomly oriented. Figure 13.6 shows that in the absence of an external field the distribution of dipole moments for the interfacial molecules has a maximum for the dipoles parallel to the interface. This preferred alignment of the water dipoles has also been found at the surface of water films on hydrophobic surfaces. It is due to the formation of a hydrogen bond network at the interface.[75,76] In this alignment, three of the four hydrogen bond acceptors/donors are oriented toward the bulk and participate in the hydrogen bond network. The resulting orientational restriction leads to an anisotropic polarizability of the droplet: if the field is perpendicular to the droplet surface, orientational polarization is accompanied by a breaking of the hydrogen bond network. The calculations show that the formation of a water bridge requires the application of a threshold field of 1.2 V/nm, which agrees with the range of values measured in AFM, $E_{\mathrm{th}} = 0.7$–$1.9\ \mathrm{V\,nm^{-1}}$.[19,53,69,72] The experimental

uncertainty is attributed to the tip's curvature, which gives rise to an inhomogeneous field decay.

In the droplet most of the water molecules at the interface are oriented perpendicular to the field. As a consequence, the orientation of the dipoles is restricted and they cannot align with the field. The polarizability of the droplet is low. At the threshold field, the outermost dipoles start aligning with the field. The alignment weakens the hydrogen bonds with the molecules underneath. However, it also triggers a process that ends in the formation of the water bridge. Once the threshold field is exceeded, most of the dipole moments are parallel to the field, the polarizability reaches its maximum and the water bridge is formed. The interfacial molecules that are forced to rotate must also minimize the interactions with the other molecules inside the drop, which would like them oriented parallel to the interface. In the bridge configuration, most of the interfacial water molecules fulfill the double requirement of forming an interfacial hydrogen bond network and being oriented in the direction of the external field.

Figure 13.7 shows four snapshots from the formation of a pillar of water molecules induced by a field of 2 V nm^{-1}. The simulation starts from a droplet of 1,014 molecules equilibrated in the absence of the field (a), where the average contact angle on a silicon dioxide surface is 40°.[53] The field perpendicular to the surface polarizes

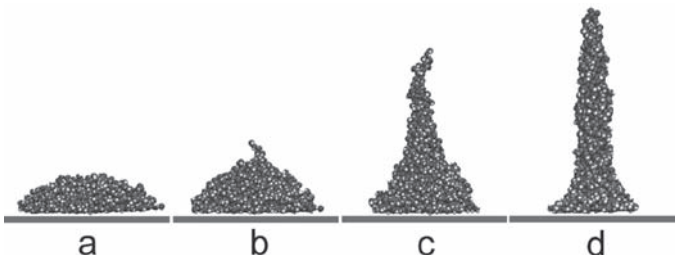

Figure 13.7 Top: molecular dynamics evolution of 1,014 water molecules in the presence of an external electric field on a hydrophilic surface (E_z = 2.0 V nm^{-1}). Panel *a* represents the equilibrated state of the droplet without an external field. Panels *b* and *c* represent, respectively, the droplet shape after 25 and 50 ps. Panel *d* represents the final shape after switching on the field. The final shape is reached at $t = 75$ ps. (Data adapted from Ref. 74.)

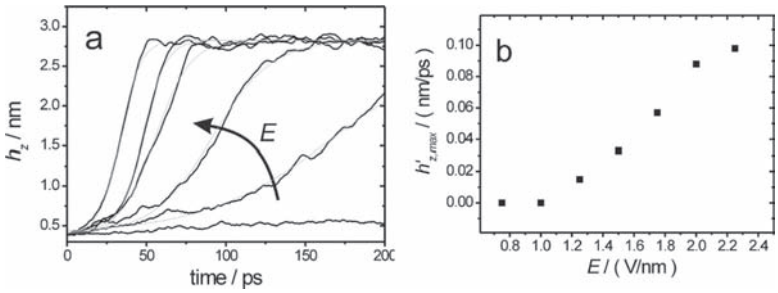

Figure 13.8 Influence of the electric field strength on the evolution of the water droplet. (a) Height increase as a function of time for several values of the electric field (2.25, 2.0, 1.75, 1.5, 1.25, 1.0 V nm^{-1}) (black lines) and fit to sigmoidal function (thin gray lines). (b) Maximum growth rate as a function of the field. The simulations were performed by using the SPC/E potential for water.[78] (Data adapted from Ref. 74.)

and distorts the outermost water layer. The drop changes shape gradually with time (b and c), and finally a water bridge is formed (d). The snapshops have been taken at 0, 25, 50, and 75 ps, respectively. The sequence of snapshots indicates that the process that leads to the formation of a water bridge, once the field strength is above the threshold value, is in the subnanosecond range.

The change of the drop height h_z perpendicular to the surface for different field strengths is shown in Fig. 13.8. At 2.25, 2.00, 1.75, 1.50, and 1.25 V, the shape of the droplet starts to change almost immediately. In contrast no tendency to form a column was observed for fields below 1.0 V even at longer time scales. Remarkably, below the threshold field the distortion observed in the droplet is of a few tenths of angstrom. The kinetics of the displacement, h_z, is sigmoidal in time. This behavior follows from the presence of the limiting factors during the growth process[77] such as the tensile strength of water, which exerts a force beyond which the pillar cannot extend.

13.3 Observation of Field-Induced Water Bridges with a Force Microscope

A force microscope operated in the amplitude modulation mode[31] offers a method to determine some of the key aspects leading to

the formation of nanoscale water bridges under the influence of an electric field. The presence of a water bridge, in fact, its associated capillary force, can be measured by detecting its effects on the cantilever tip's dynamics.[19,53]

A common experimental setup to observe the formation of field-induced water bridges involves enclosing the atomic force microscope head and base into a closed box with inlets for dry and H_2O-saturated nitrogen.[53] The use of doped n+–type silicon cantilevers are recommended to avoid resistance losses in the tip. Typical values of the force constant and the resonant frequency are, respectively, about 30 N/m and 300 kHz. The cantilever is excited at its resonant frequency to benefit from the maximum amplification conditions. Silicon surfaces such as *p*-type Si(100) with a resistivity of 14 Ωcm are good candidates to observe water bridges. Due to exposure to air, those surfaces have a very thin native oxide layer of about 1 nm. That surface is slightly hydrophilic due to the presence of OH groups. On the other hand, the native oxide layer does not interfere with the observations. To monitor the cantilever movement in real time, the signal from the photodiode is analyzed in an oscilloscope. To avoid an initial tip–sample surface contact, and thus the unintended formation of a water bridge, the atomic force microscope is operated in the noncontact regime of amplitude modulation AFM.[31,79] The protocol to form field-induced water bridges with an atomic force microscope requires several steps. First, the relative humidity is stabilized at a fixed value, usually in the 40%–50% range. Then, the force microscope tip is oscillated at a fixed distance from the surface. The closest tip–surface distance at the bottom part of the oscillation is 1–2 nm. Finally, a voltage pulse is applied between the tip (grounded) and the sample surface.

Figure 13.9 shows the tip's oscillation before, during, and after the application of a voltage pulse. Two situations are shown. The top panel shows the tip's oscillation for a voltage pulse just below V_{th}, while the bottom panel shows the tip's oscillation for a voltage pulse just above V_{th}. In the plot the instantaneous cantilever deflection is represented by a dot and the black line represents the voltage pulse. The top panel shows that when the pulse is on (II), the electric field deflects the mean position of the tip and reduces its amplitude. Once the pulse is off, the tip oscillation recovers its initial amplitude (I).

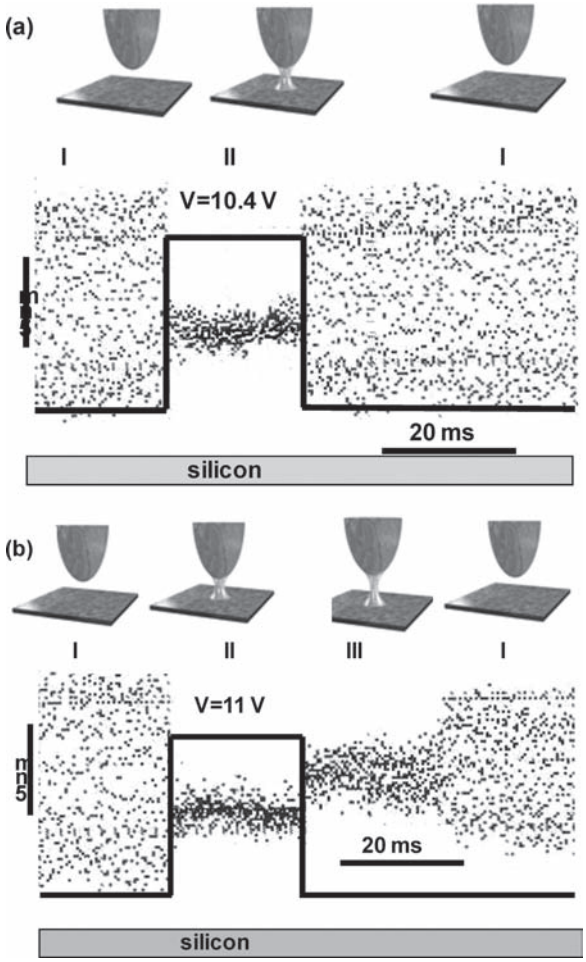

Figure 13.9 Observation of a field-induced water bridge with amplitude modulation AFM. (a) Depicts the tip's oscillation before, during, and after the application of a voltage pulse for 20 ms that did not involve the formation of a water bridge ($V = 10.4$ V). (b) Depicts the tip's oscillation before, during, and after the application of a voltage pulse for 20 ms that involved the formation of a water bridge ($V = 11$ V). Step III is indicative of the formation of a water bridge because the oscillation does not recover its initial value once the pulse is off. Each dot in the oscilloscope traces represents an instantaneous position of the atomic force microscope tip. (Data adapted from Refs. 19, 53, 69, and 81.)

However, when the voltage pulse is slightly increased from 10.4 V to 11 V, a different behavior is observed. During the application of pulse (bottom panel) the electric field deflects the mean position of the tip and reduces its amplitude (II) similar to the previous case. However, here after turning the pulse off, the amplitude remains reduced and the tip mean position is slightly deflected toward the surface (III). This indicates the presence of an additional attractive force between the tip and the silicon surface. Because the effect disappears by lowering the relative humidity, it is deduced that the capillary force is the origin of the behavior observed in step III. Consequently, step III is the signature of the formation of a liquid bridge. Finally when the meniscus is broken, for example, by retracting the tip, the amplitude, and the average deflection recover their initial values in time $(QT/\pi) \approx 1$ ms (I). This method enables to determine the threshold voltage for a given interface, relative humidity, and temperature by finding the minimum voltage that gives rise to the presence of step III. The method also allows to observe the hysteresis of the water bridge as a function of the voltage. The same method has been applied to observe the formation of ethanol, propanol, and octane bridges by filling the atomic force microscope chamber with their respective vapors.[80,81]

The above method also enables to determine the size of the water bridge. This is achieved by measuring the separation at which the water bridge becomes unstable (snap-off separation). First, the water bridge is formed as explained previously. Then the tip and the surface are separated while the oscillation is monitored with an oscilloscope. At the snap-off separation there is a sudden increase of the amplitude. This indicates that the water bridge has been broken. Then the microscope operation is reestablished, and the tip recovers its initial amplitude.[53] Figure 13.10 shows the protocol to measure the snap-off separation. From the snap-off separation, the size of the water bridge can be determined by using the expression,[53,81,82]

$$W = 2\,(R + r_1 + h_0)\sin\phi \tag{13.16}$$

with

$$\sin\varphi = \frac{r_1 + r}{R + r_1 + h_0} \tag{13.17}$$

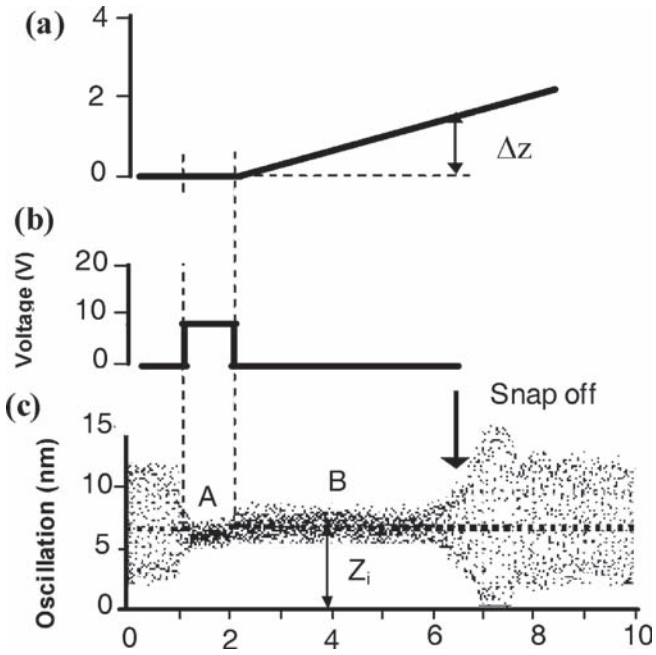

Figure 13.10 Measurement of the snap-off separation with an amplitude modulation AFM. (a) Piezo displacement Δzvs. time. (b) Voltage pulse. (c) Tip oscillation. Z_{i} represents the average tip–sample distance. The snap-off separation is given by $D_{\mathrm{snap-off}} = Z_{\mathrm{i}} + \Delta z_{\mathrm{snap-off}}$. The zero position in the y-axis represents the position of the surface. Relative humidity, $RH = 55\%$. Voltage pulse of 9 V and 1 ms. (Data adapted from Ref. 53.)

where ϕ is the filling angle and r is the bridge radius in its narrowest section. Figure 13.11 provides an explanation of the different parameters that appear in Eqs. 13.16 and 13.17.

Figure 13.12 shows the dependence of the snap-off separation and the bridge diameter as a function of the pulse duration ($V = 24$ V). The snap-off separation and the bridge diameter grow logarithmically with the time. This indicates that the pulse times used to form the bridge are smaller than those required to achieve its equilibrium size. This result might be at variance with some kinetics studies of capillary condensation in nanopores in the absence of an external field.[13,59–61] Some of those studies show that the

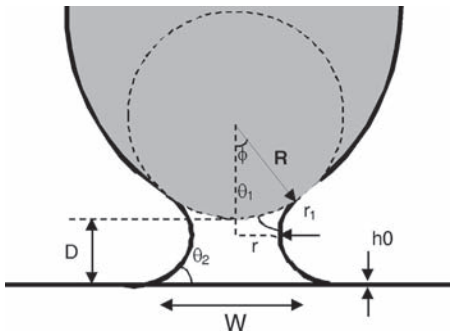

Figure 13.11 Schematics of a concave water meniscus formed between a sphere and a flat surface; θ_1 and θ_2 are the wetting angles, ϕ is the filling angle, D is the tip–sample separation, R is the tip radius, r_1 is one of the main curvature radius, r is the water neck radius at its narrowest section, and h_0 is the water thickness adsorbed on the sample surface.

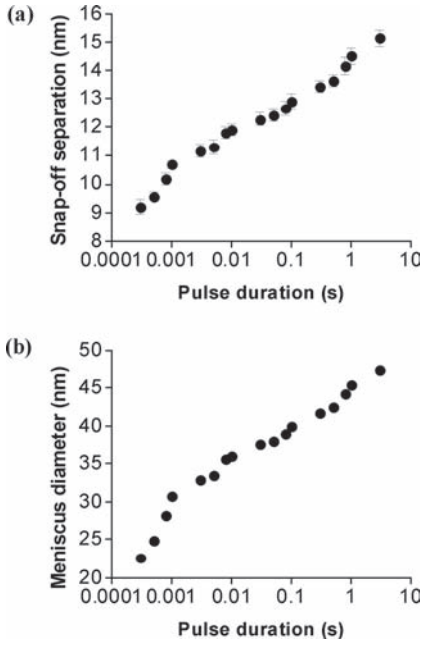

Figure 13.12 (a) Dependence of the snap-off separation on the voltage pulse duration. (b) Dependence of the water bridge diameter on the pulse duration. Data obtained from the snap-off separation measurements presented in (a). The sample is biased negatively with respect to the tip. $RH = 40\%$, $V = 24$ V, and $R = 30$ nm. (Data adapted from Ref. 53.)

time scale over which spontaneously formed capillaries reach their equilibrium sizes may be below one second.[13,61]

13.4 Tip-Based Oxidation Nanolithography

Tip-based oxidation nanolithography, also known as AFM or local oxidation nanolithography, provides a remarkable example of the use of nanoscale water bridges for patterning and device fabrication.[51] AFM oxidation nanolithography is based on the spatial confinement of an anodic oxidation between the tip and the sample surface. The oxidation process is mediated by the formation of a nanoscale water bridge (Fig. 13.13). In fact, due to the sequential character of AFM, the generation of a nanopattern might involve the formation of multiple water bridges. This bridge acts as a nanoscale electrochemical cell that usually contains more than 10^5 water molecules (Fig. 13.14). The polarity of the voltage is in such a way that the tip acts as the cathode (negative) and the sample surface

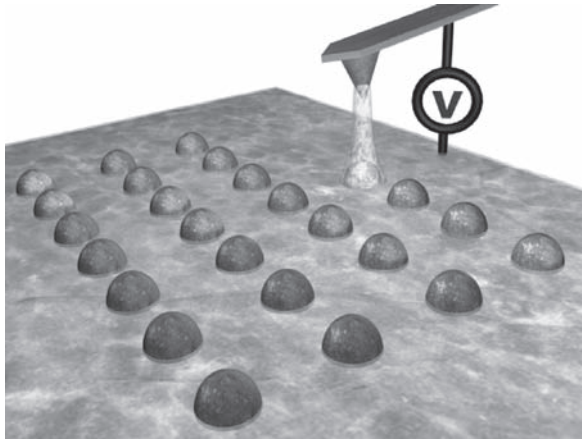

Figure 13.13 Scheme of patterning in AFM oxidation nanolithography. The atomic force microscope tip is placed 1–5 nm above the surface. The application of a voltage pulse induces the formation of a water bridge and activates the anodic oxidation of the surface. During the nanolithography, the atomic force microscope switches back and forward from the imaging mode to the nanolithography mode.

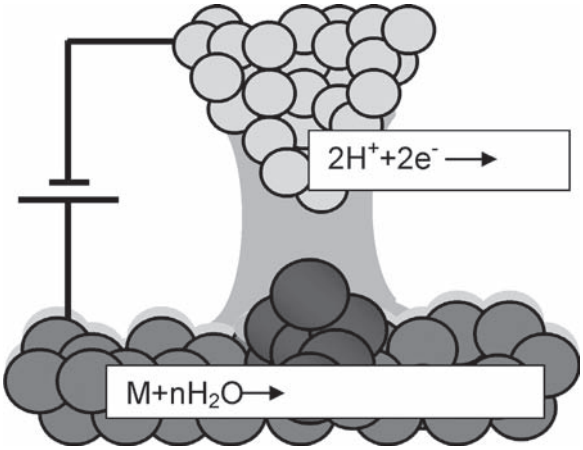

Figure 13.14 Some of the electrochemical reactions involved in a local oxidation experiment. The water bridge provides the oxyanions and confines the spatial extent of the reaction.

is the anode (positive). Tip-based oxidation nanolithography can be either performed with the tip in contact with the sample surface or in a noncontact mode.[84] In the later case, the formation of a water bridge requires the application of a voltage (see previous sections). Noncontact AFM oxidation enhances the tip's lifetime for nanofabrication purposes with respect to experiments performed with AFM in contact mode.

The electric field has three roles in tip-based oxidation. First, it induces the formation of the water bridge. Second, it generates the oxyanions needed for the oxidation by decomposing water molecules. Third, it drives the oxyanions to the sample interface and facilitates the oxidation process. The technique generates ultrasmall silicon oxide nanostructures with a lateral size of about 5 nm and a height in the 1 to 5 nm range.

Tip-based oxidation experiments were first performed on Si(111) and polycrystaline tantalum faces.[85,86] Since then a large number of materials have been locally oxidized, such as compound III–V semiconductors; silicon carbide; several metals such as titanium, tantalum, aluminum, molybdenum, nickel, and niobium; perovskite manganite thin films; dielectrics such as silicon nitride

films as well as organosilane self-assembled monolayers; dendritic objects; and carbonaceous films.[51,87]

In AFM oxidation, the height and width of the oxide depend linearly on the voltage. The height also shows a power law dependence with the pulse time *t*of the type

$$\text{height} \approx (t/t_0)^{\alpha} \tag{13.18}$$

where α is in the 0.1–0.3 range for Si(100) surfaces. Voltage pulses usually change from experiment to experiment, but they are, respectively, in the 10–30 V and 0.005–1 second ranges. The local oxidation process is accompanied by an extremely small current.[45,88] The value depends on the final dot size. Common values are in the subpicoampere regime. Experimental observations have shown that the current measured during the oxidation process matches the current calculated from the volume of the nanostructure. To achieve this result, it was considered that four elementary charges are needed to oxidize one Si atom.

13.4.1 *Nanopatterning and Nanodevices*

Masks, thin insulating barriers, or templates are the elements directly fabricated by AFM oxidation nanolithography. However, a combination of these elements enables the fabrication of a wide variety of nanoscale patterns and nanomechanical or nanolectronic devices.

Figures 13.15 and 13.16 show two examples that underline the flexibility and robustness of this technique for nanofabrication. Figure 13.15a shows the steps to build molecular architectures by combining top-down nanolithography and self-assembled methods. In this case, single molecules of ferritin have been deposited on silicon surfaces with an accuracy similar to the size of the molecules ($\approx$10 nm).[89] First, the silicon surface is covered with a self-assembled monolayer of aminopropyltriethoxysilane (APTES), and then a region is locally oxidized with the atomic force microscope tip. The oxidation process also removes the monolayer under the tip. The nanostripe before the deposition of ferritin molecules is shown in Fig. 13.15b, while Fig. 13.15c shows a densely packed distribution of proteins on the nanostripe. The

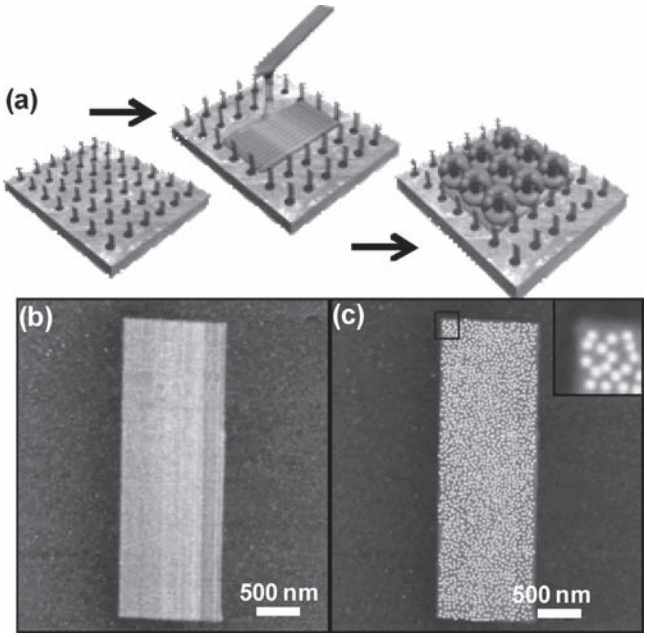

Figure 13.15 Patterning of ferritin molecules by combining AFM oxidation nanolithography and silicon functionalization at low pH values. (a) Steps of the nanopatterning process. (b) AFM image of a local oxide pattern. (c) High-density packing of ferritin molecules on the nanopattern. The inset shows the distribution of the proteins in the marked region. (Data adapted from Ref. 89.)

ferritin molecules form a nonperiodic structure with an average molecule–molecule distance of 20 nm. The total absence of ferritin molecules outside the patterned stripe is remarkable. This result underlines the strong selectivity of the patterning process. In other experiments one-dimensional arrays of individual ferritin molecules have been accurately patterned over a submicrometer region of the macroscopic silicon surface.

Sophisticated nanolectronic devices such as SiNW transistors and circuits have been fabricated by AFM oxidation nanolithography.[54,90] In this application, AFM oxidation generates a narrow oxide mask on top of the active layer of a silicon-on-insulator substrate. The unmasked silicon layer is then removed by using

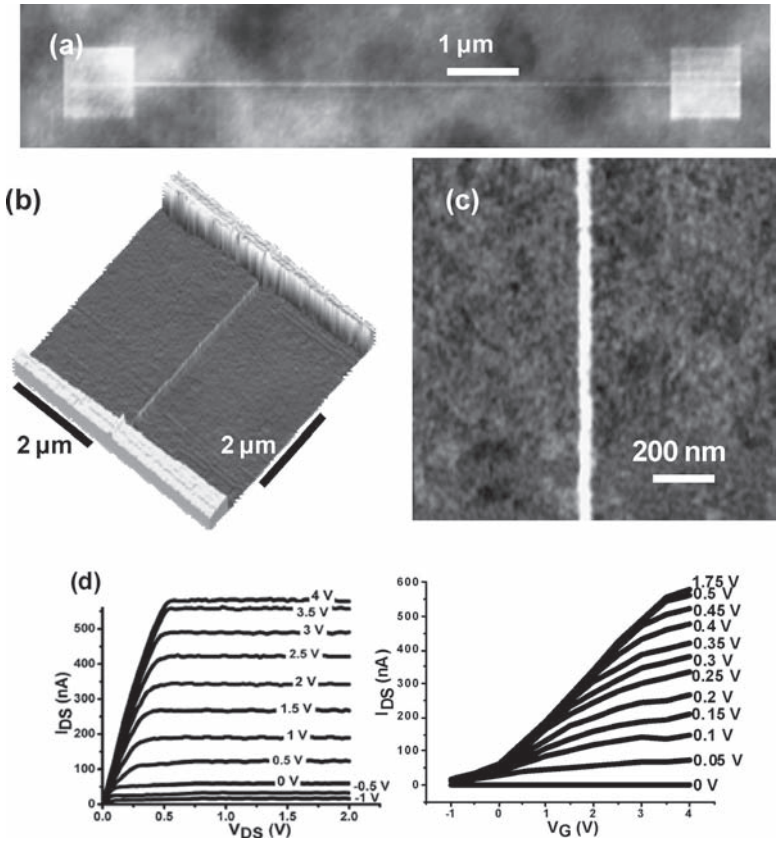

Figure 13.16 SiNW transistor fabricated by AFM oxidation nanolithography. (a) AFM image of a local oxide pattern to be used as mask. (b) AFM image of the SiNW connected to two platinum electrodes. (c) High-resolution image of the SiNW shown in (b). (d) Output (left) and transfer (right) and characteristics of the SiNW transistor. (Data adapted from Ref. 90.) *Abbreviation*: SiNW, silicon nanowire.

wet or dry chemical etching procedures. The local oxide protects the underneath silicon from the etching. This leaves a single-crystalline SiNW with a top width that matches the width of the oxide mask. The bottom width of the nanowire will depend on the etching method used. Sharper features are obtained by using plasma etching methods. Finally, the SiNW is contacted to a micrometer-

size platinum source and drain contacts by either photolithography or electron beam lithography. After metallization, the sample might be annealed for 30 minutes at 500°C to improve the electrical properties of the contacts. In this way very small SiNWs have been fabricated, in particular SiNWs with a channel width of 4 nm.[54]

Figure 13.16 shows a SiNW 4 μm in length and 9.5 nm in width. Figure 13.16a shows the silicon oxide mask. The thickness of the fabricated mask is about 3 nm. After etching, the SiNW is contacted to two platinum electrodes (Fig. 13.16b). The fabricated SiNW is the main element of a field-effect transistor formed by introducing a gate electrode. Here, the gate electrode is situated at the back of a silicon-on-insulator wafer. The output and transfer characteristics of the transistor formed with the SiNW described above are shown in Fig. 13.16d. The output curve (left panel) shows a clear dependence on the gate voltage. The off-state drain current leakage is about 10^{-11} A. The device shown above has an on/off current ratio of 10^5, and it can be used to develop very sensitive biomolecular sensors.

13.4.2 *Parallel Patterning by Using Liquid Bridges*

The sequential character of AFM somehow limits the technological applications of tip-based nanolithographies, in particular AFM oxidation. In addition, the patterning area is limited by the AFM scanner, which usually has a range of 10–50 microns. To overcome these limitations, several methods have been proposed to upscale the local oxidation process by using a conductive stamp with multiple protrusions as the cathode electrode[91–95] (Fig. 13.17a). Then, in a single step a large area could be patterned with millions of nanostructures.

Figure 13.17 shows AFM images of the stamp (b) and its replica (c). In particular, the replica shows a region of 20.8×20.8 μm^2 that contains 29 stripes with a periodicity of 740 nm. The lines were generated by pressing the stamp on the silicon substrate in an atmosphere saturated with octane vapor and by applying a voltage pulse of 36 V for one minute. In this case, the pattern periodicity was established by the stamp periodicity, a gold-coated DVD sample with a periodicity of 740 nm. Because the liquid bridges were made of octane, the chemical composition of the fabricated nanostructures

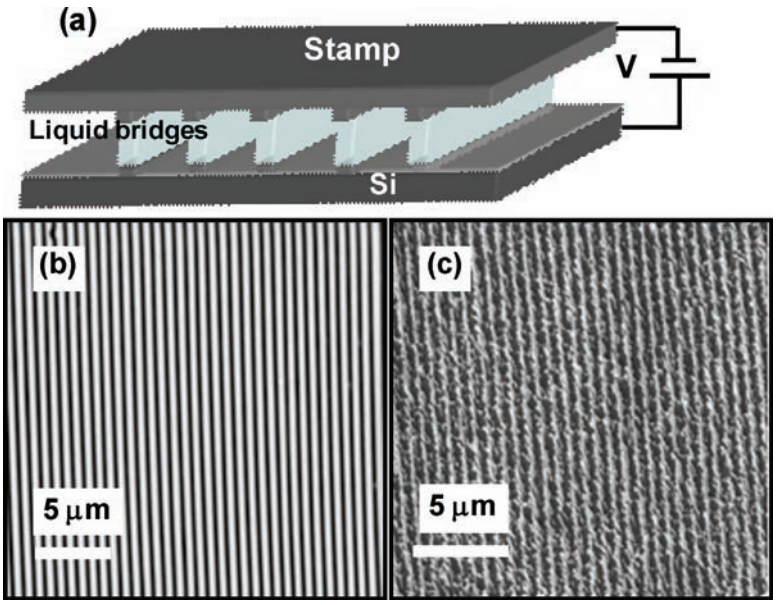

Figure 13.17 Scheme of parallel nanopatterning by using field-induced liquid bridges. (a) AFM image of a region of the gold-coated DVD stamp used for parallel patterning. (b) AFM image of an array of polymer lines fabricated in parallel by using the stamp shown in (a). The pattern periodicity of the replica is 740 nm, which coincides with the stamp periodicity. In this case, the bridges were formed by octane. (Data adapted from Ref. 81.)

are no longer oxides but made of a carbon-rich material. The use of liquid bridges of different chemical compositions illustrates the general character of the method exposed in this chapter to form and manipulate liquid bridges by using electric fields.

13.5 Summary

The control and manipulation of nanoscale liquid bridges or capillaries, in particular water capillaries, play a crucial role in several high-resolution lithography methods. There the liquid bridge provides the spatial confinement of a chemical reaction, which causes a local modification of the surface. The bridge also supplies the chemicals for the reaction to happen. Electric fields

provide useful methods to generate, control, and manipulate the geometry of nanoscale liquid bridges.

Acknowledgments

I am very grateful to Francesco Zerbetto, Tobias Cramer, Juan José Saenz, Monserrat Calleja and Antonio Garcia-Martin for the fruitful and stimulating discussions aimed to elucidate the behavior of water in electric fields. I acknowledge the financial supports from Ministerio de Ciencia, Investigación e Innovación (MAT2009-08650).

References

1. A. W. Adamson, *Physical Chemistry of Surfaces*. New York: John Wiley and Sons (1990).
2. P. G. de Gennes, F. Brochard-Wyart, and D. Queré, *Capillarity and Wetting Phenomena: Drops*, *Bubbles*, *Pearls*, *Waves*. New York: Springer Science (2004).
3. P. W. Atkins, *Physical Chemistry*. 4th ed. New York: W.H. Freeman (1990).
4. J. Israelachvili, *Intermolecular and Surface Forces*. London: Academic Press (1994).
5. P. J. Feibelman, The first wetting layer on a solid, *Phys. Today*, **63**, 34–39 (2010).
6. A. Verdaguer, G. M. Sacha, H. Bluhm, and M. Salmeron, Molecular structure of water at interfaces: wetting at the nanometer scale, *Chem. Rev.*, **106**, 1478 (2006).
7. L. R. Fisher and J. N. Israelachvili, Experimental studies on the applicability of the Kelvin equation to highly curved concave menisci, *Colloids Surf.*, **3**, 303 (1981).
8. H. K. Christenson, Capillary condensation due to van-der-Waals attraction in wet slits, *Phys. Rev. Lett.*, **73**, 1821–1824 (1994).
9. R. Digilov, Kelvin equation for meniscuses of nanosize dimensions, *Langmuir*, **16**, 1424–1427 (2000).
10. C. M. Mate, Application of disjoining and capillary pressure to liquid lubricant films in magnetic recording, *J. Appl. Phys.*, **72**, 3084 (1992).

11. R. W. Carpick, D. F. Ogletree, and M. Salmeron, Lateral stiffness: a new nanomechanical measurement for the determination of shear strengths with friction force microscopy, *Appl. Phys. Lett.*, **70**, 1548–1550 (1997).
12. M. Binggeli and C. M. Mate, Influence of capillary condensation of water on nanotribology studied by force microscopy, *Appl. Phys. Lett.*, **65**, 415–417 (1994).
13. L. Sirghi, R. Szoszkiewicz, and E. Riedo, Volume of a nanoscale water bridge, *Langmuir*, **22**, 1093 (2006).
14. R. C. Major, J. E. Houston, M. J. McGrath, J. I. Siepmann, and X. Y. Zhu, Viscous water meniscus under nanoconfinement, *Phys. Rev. Lett.*, **96**, 177803–177806 (2006).
15. L. Nony, T. Cohen-Bouhacina, and J. P. Aime, Dissipation induced by attractive interaction in dynamic force microscopy: contribution of adsorbed water layers, *Surf. Sci.*, **499**, 152–160 (2002).
16. H. Gau, S. Herminghaus, P. Lenz, and R. Lipowsky, Liquid morphologies on structured surfaces: from microchannels to microchips, *Science*, **283**, 46–49 (1999).
17. R. Lipowsky, Morphological wetting transitions at chemically structured surfaces, *Curr. Opin. Coloid Interface Sci.*, **6**, 40–48 (2001).
18. L. Fabie, H. Durou, and T. Ondarcuhu, Capillary forces during liquid nanodispensing, *Langmuir*, **26**, 1870–1878 (2010).
19. R. Garcia, M. Calleja, and H. Rohrer, Patterning of silicon surfaces with noncontact atomic force microscopy: field-induced formation of nanometer-size water bridges, *J. Appl. Phys.*, **86**, 1898–1903 (1999).
20. H. Heinzelmann, A. Meister, P. Niedermann, J. Bitterli, J. Polesel-Maris, M. Liley, M. Gabi, P. Behr, P. Studer, J. Voros, and T. Zambelli, NADIS: a novel AFM-based tool for dispensing fluids into single cells, *Microsc. Anal.*, **26**, 11–13 (2009).
21. M. Cavallini, C. Albonetti, and F. Biscarini, Nanopatterning soluble multifunctional materials by unconventional wet lithography, *Adv. Mater.*, **21**, 1043–1053 (2009).
22. A. L. Weisenhorn, P. K. Hansma, T. R. Albrecht, and C. F. Quate, Forces in AFM in air and water, *Appl. Phys. Lett.*, **54**, 2651–2653 (1989).
23. T. Thundat, X. Y. Zheng, G. Y. Chen, and R. J. Warmack, Role of the relative humidity in AFM, *Surf. Sci. Lett.*, **294**, L939–L943 (1993).
24. T. Stiffer, O. Marti, and B. Bhushan, Theoretical investigation of the distance dependence of capillary and van der Waals forces in scanning force microscopy, *Phys. Rev. B*, **62**, 13667–13673 (2000).

25. J. Colchero, A. Storch, M. Luna, J. Gómez-Herrero, and A. M. Baró, Observation of liquid neck formation with scanning force microscopy techniques, *Langmuir*, **14**, 2230–2234 (1998).
26. L. Zitzler, S. Herminghaus, and F. Mugele, Capillary forces in tapping mode atomic force microscopy, *Phys. Rev. B*, **66**, 155436 (2002).
27. H. Choe, M. H. Hong, Y. Seo, K. Lee, G. Kim, Y. Cho, J. Ihm, and W. Jhe, Formation, manipulation, and elasticity measurement of a nanometric column of water molecules, *Phys. Rev. Lett.*, **95**, 187101–187104 (2005).
28. Y. M. Men, X. R. Zhang, and W. C. Wang, Capillary liquid bridges in atomic force microscopy: formation, rupture and hysteresis, *J. Chem. Phys.*, **131**, 184702 (2009).
29. Q. Zhong, D. Inniss, K. Kjoller, and V. B. Elings, Fractured polymer/silica fiber surface studied by tapping mode atomic force microscopy, *Surf. Sci. Lett.*, **290**, L688–L692 (1993).
30. J. Tamayo and R. Garcia, Deformation, contact time and phase contrast in tapping mode scanning force microscopy, *Langmuir*, **12**, 4430–4435 (1999).
31. R. Garcia and R. Perez, Dynamic atomic force microscopy methods, *Surf. Sci. Rep.*, **47**, 197–302 (2002).
32. R. D. Piner, J. Zhu, F. Xu, S. H. Hong, and C. A. Mirkin, Dip-pen nanolithography, *Science*, **283**, 661–663 (1999).
33. Y. Li, B. W. Maynor, and J. Liu, Electrochemical AFM "dip-pen" nanolithography, *J. Am. Chem. Soc.*, **123**, 2105–2106 (2001).
34. M. Cavallini and F. Biscarini, Nanostructuring conjugated materials by lithographically controlled wetting, *Nano Lett.*, **3**, 1269–1271 (2003).
35. M. Cavallini, I. Bergenti, S. Milita, G. Ruani, I. Salitros, Z. R. Qu, R. Chandrasekar, and M. Ruben, Micro- and nanopatterning of spin-transition compounds into logical structures, *Angew. Chem., Int. Ed.*, **47**, 8596–8600 (2008).
36. W. L. Cheng, N. Y. Park, M. T. Walter, M. R. Hartman, and D. Luo, Nanopatterning self-assembled nanoparticle superlattices by moulding microdroplets, *Nat. Nanotech.*, **3**, 682–690 (2008).
37. R. V. Martinez, J. Martinez, M. Chiesa, R. Garcia, E. Coronado, E. Pinilla-Cienfuegos, and S. Tatay, Large-scale nanopatterning of single proteins used as carriers of magnetic nanoparticles, *Adv. Mater.*, **22**, 588 (2010).
38. A. Meister, M. Liley, J. Brugger, R. Pugin, and H. Heinzelmann, Nanodispenser for attoliter volume deposition using atomic force microscopy probes modified by focused-ion-beam milling, *Appl. Phys. Lett.*, **85**, 6260–6262 (2004).

39. A. Meister, M. Gabi, P. Behr, P. Studer, J. Voros, P. Niedermann, J. Bitterli, J. Polesel-Maris, M. Liley, H. Heinzelmann, and T. Zambelli, Combining atomic force microscopy and nanofluidics in a universal liquid delivery system for single cell applications and beyond, *Nano Lett.*, **9**, 2501–2507 (2009).
40. L. Fabie, H. Durou, and T. Ondarcuhu, Capillary forces during liquid nanodispensing, *Lagmuir*, **26**, 1870–1878 (2010).
41. J. A. Dagata, Device fabrication by scanned probe oxidation, *Science*, **270**, 1625–1626 (2010).
42. J. A. Dagata, F. Perez-Murano, C. Martin, H. Kuramochi, and H. Yokoyama, Current, charge, and capacitance during scanning probe oxidation, *J. Appl. Phys.*, **96**, 2386–2392 (2004).
43. E. S. Snow and P. M. Campbell, AFM fabrication of sub-10-nanometer metal-oxide devices with in situ control of electrical properties, *Science*, **270**, 1639–1641 (1995).
44. O. P. Khatri, J. Han, T. Ichii, K. Murase, and H. Sugimura, Self-assembly guided one-dimensional arrangement of gold nanoparticles: a facile approach, *J. Phys. Chem. C*, **112**, 16182–16185 (2008).
45. H. Kuramochi, K. Ando, T. Tokizaki, and H. Yokoyama, In situ detection of faradaic current in probe oxidation using a dynamic force microscope, *Appl.Phys. Lett.*, **84**, 4005–4007 (2004).
46. V. Bouchiat, M. Faucher, C. Thirion, W. Wernsdorfer, F. Fournier, and B. Pannetier, Josephson junctions and superconducting quantum interference devices made by local oxidation of niobium ultrathin films, *Appl. Phys. Lett.*, **79**, 123–125 (2001).
47. C. F. Chen, S. D. Tzeng, H. Y. Chen, and S. Gwo, Silicon microlens structures fabricated by scanning-probe gray-scale oxidation, *Opt. Lett.*, **30**, 652–654 (2005).
48. L. Pellegrino, M. Biasotti, M. Bellingeri, C. Bernini, A. S. Siri, and D. Marré, All-oxide crystalline microelectromechanical systems, *Adv. Mater.*, **21**, 2377–2381 (2009).
49. L. Pellegrino, Y. Yanagisawa, M. Ishikawa, T. Matsumoto, H. Tanaka, and T. Kawai, $(Fe, Mn)_3O_4$ nanochannels fabricated by AFM local-oxidation nanolithography using Mo/poly(methyl methacrylate) nanomasks, *Adv. Mater.*, **18**, 3099 (2006).
50. N. Rochdi, D. Tonneau, F. Jandard, H. Dallaporta, V. Safarov, and J. Gautier, Electrical conductivity of ultra-thin silicon nanowires, *J. Vac. Sci. Technol. B*, **26**, 159–163 (2008).

51. R. Garcia, R. V. Martinez, and J Martinez, Nano-chemistry and scanning probe nanolithographies, *Chem. Soc. Rev.*, **35**, 29–38 (2006) and references therein.
52. M. Tello and R. Garcia, Nano-oxidation of silicon surfaces: comparison of noncontact and contact atomic force microscopy methods, *Appl. Phys. Lett.*, **79**, 424–426 (2001).
53. M. Calleja, M. Tello, and R. Garcia, Size determination of field-induced water menisci in noncontact atomic force microscopy, *J. Appl. Phys.*, **92**, 5539–5542 (2002).
54. J. Martinez, R. V. Martinez, and R. Garcia, Silicon nanowire transistors with a channel width of 4 nm fabricated by atomic force microscope nanolithography, *Nano Lett.*, **8**, 3636–3639 (2008).
55. C. R. Kinser, M. J. Schmitz, and M. C. Hersam, Kinetics and mechanism of atomic force microscope local oxidation on hydrogen-passivated silicon in inert organic solvents, *Nano Lett.*, **5**, 91–95 (2005).
56. R. Maoz, E. Frydman, S. R. Cohen, and J. Sagiv, "Constructive nanolithography": inert monolayers as patternable templates for in-situ nanofabrication of metal-semiconductor-organic surface structures—a generic approach, *Adv. Mater.*, **12**, 725 (2000).
57. S. Hoeppener, R. Maoz, S. R. Cohen, L. Chi, H. Fuchs, and J. Sagiv, Metal nanoparticles, nanowires, and contact electrodes self-assembled on patterned monolayer templates—a bottom-up chemical approach, *Adv. Mater.*, **14**, 1036 (2002).
58. S. T. Liu, R. Maoz, G. Schmid, and J. Sagiv, Template guided self-assembly of [Au5(5)] clusters on nanolithographically defined monolayer patterns, *Nano Lett.*, **2**, 1055–1060 (2002).
59. M. M. Kohonen, N. Maeda, and H. K. Christenson, Kinetics of capillary condensation in a nanoscale pore, *Phys. Rev. Lett.*, 82, 4667–4670 (1999).
60. M. M. Kohonen and H. K. Christenson, Capillary condensation of water between rinsed mica surfaces, *Langmuir*, **16**, 7285–7288 (2000).
61. R. Szoszkiewicz and E. Riedo, Nucleation time of nanoscale water bridges, *Phys. Rev. Lett.*, **95**, 135502 (2005).
62. A. Klinger, H. Herminghaus, and F. Mugele, Self-excited oscillatory dynamics of capillary bridges in electric fields, *Appl. Phys. Lett.*, **82**, 4187–4189 (2003).
63. F. Mugele and J. C. Baret, Electrowetting: from basics to applications, *J. Phys.: Condens. Matter*, **17**, R705–R774 (2005).

64. C. Quilliet and B. Berge, Electrowetting: a recent outbreak, *Curr. Opin. Colloid Interface Sci.*, **6**, 34–39 (2001).
65. R. Gupta, G. K. Olivier, and J. Frechette, Invariance of the solid-liquid interfacial energy in electrowetting probed via capillary condensation, *Langmuir*, **26**, 11946–11950 (2010).
66. N. Kurra, A. Scott, and G. U. Kulkarni, Electrodeposition and evaporation of atoliter water droplets: direct visualization using atomic force microscopy, *Nano Res.*, **3**, 307–316 (2010).
67. I. C. Yeh and M. L. Berkowitz, Dielectric constant of water at high electric fields: molecular dynamics study, *J. Chem. Phys.*, **110**, 7935–7942 (1999).
68. J. Buehrle, S. Herminghaus, and F. Mugele, Interface profiles near three-phase contact lines in electric fields, *Phys. Rev. Lett.*, **91**, 086101–086104 (2003).
69. S. Gomez-Monivas, J. J. Saenz, M. Calleja, and R. Garcia, Field-induced formation of nanometer-sized water bridges, *Phys. Rev. Lett.*, **91**, 056101 (2003).
70. S. Djurkovic, C. B. Clemons, D. Golovaty, and G. W. Young, Effects of the electric field shape on nano-scale oxidation, *Surf. Sci.*, **601**, 5340–5358 (2007).
71. P. B. Paramonov and S. F. Lyksyutov, Density-functional description of water condensation in proximity of nanoscale aperity, *J. Chem. Phys.*, **123**, 084705 (2005).
72. G. M. Sacha, A. Verdaguer, and M. Salmeron, Induced water condensation and bridge formation by electric fields in atomic force microscopy, *J. Phys. Chem.*, **110**, 14870–14873 (2006).
73. A. Garcia-Martin and R. Garcia, Formation of nanoscale liquid menisci in electric fields, *Appl. Phys. Lett.*, **88**, 123115 (2006).
74. T. Cramer, F. Zerbetto, and R. Garcia, Molecular mechanism of water bridge buildup: field-induced formation of nanoscale menisci, *Langmuir*, **24**, 6116–6120 (2008).
75. X. Xia and M. L. Berkowitz, Electric-field-induced restructuring of water at a platinum water interface—a molecular-dynamics computer-simulation, *Phys. Rev. Lett.*, **74**, 3193–3196 (1995).
76. S. J. Suresh, A. V. Satish, and A. Choudhary, Influence of electric field on the hydrogen bond network of water, *J. Chem. Phys.*, **124**, 074506 (2006).
77. F. Lugli, S. Höfinger, and F. Zerbetto, The collapse of nanobubbles in water, *J. Am. Chem. Soc.*, **127**, 8020–8021 (2005).

78. H. J. C. Berendsen, J. R. Grigera, and T. P. Straatsma, The missing term in effective pair potentials, *J. Phys. Chem.*, **91**, 6269–6271 (1987).
79. R. Garcia and A. San Paulo, Attractive and repulsive tip-sample interaction regimes in tapping-mode atomic force microscopy, *Phys. Rev. B*, **60**, 4961–4967 (1999).
80. M. Tello and R. Garcia, Giant growth rate in nano-oxidation of p-silicon surfaces by using ethyl alcohol liquid bridges, *Appl. Phys. Lett.*, **83**, 2339–2341 (2003).
81. R. V. Martinez and R. Garcia, Nanolithography based on the formation and manipulation of nanometer-size organic liquid menisci, *Nano Lett.*, **5**, 1161–1164 (2005).
82. F. M. Orr, L. E. Scriven, and A. P. Rivas, Pendular rings between solids. Meniscus properties and capillary force, *J. Fluid. Mech.*, **67**, 723–742 (1975).
83. E. Bayramli, A. Abou-Obeid, and T. G. M. Vam de Ven, Liquid bridges between spheres in a gravitational-field, *J. Colloid. Interface Sci.*, **116**, 490–502 (1987).
84. M. Tello and R. Garcia, Nano-oxidation of silicon surfaces: comparison of non-contact and contact atomic force microscopy methods, *Appl. Phys. Lett.*, **79**, 424–426 (2001).
85. J. A. Dagata, J. Schneir, H. H. Harary, C. J. Evans, M. T. Postek, and J. Bennett, Modification of hydrogen-passivated silicon by a scanning tunneling microscope operated in air, *Appl. Phys. Lett.*, **56**, 2001–2003 (1990).
86. T. Thundat, L. A. Nagahara, P. I. Oden, S. M. Lindsay, M. A. George, and W. S. Glaunsinger, Modification of tantalum surfaces by STM in an electrochemical cell, *J. Vac. Sci. Technol., A,* **8**, 3537–3541 (1990).
87. A. A. Tseng, A. Notargiocomo, and T. P. Chen, Nanofabrication by scanning probe microscope lithography: a review, *J. Vac. Sci. Technol., B*, **23**, 877–894 (2005).
88. P. Avouris, T. Hertel, and R. Martel, Atomic force microscope tip-induced local oxidation of silicon: kinetics, mechanism and nanofabrication, *Appl. Phys. Lett.*, **71**, 285–287 (1997).
89. R. V. Martinez, J. Martinez, M. Chiesa, R. Garcia, E. Coronado, E. Pinilla-Cienfuegos, and S. Tatay, Large-scale nanopatterning of single proteins used as carriers of magnetic nanoparticles, *Adv. Mater.*, **22**, 588 (2010).
90. R. V. Martinez, J. Martinez, and R. Garcia, Silicon nanowire circuits fabricated by AFM oxidation nanolithography, *Nanotechnology*, **21**, 245301–245306 (2010).

91. M. Cavallini, P. Mei, F. Biscarini, and R. Garcia, Parallel writing by local oxidation nanolithography with submicrometer resolution, *Appl. Phys. Lett.*, **83**, 5286–5288 (2003).
92. N. S. Losilla, J. Martinez, and R. Garcia, Large area nanoscale patterning of silicon surfaces by parallel local oxidation, *Nanotechnology*, **20**, 475304 (2009).
93. C. Albonetti, J. Martinez, N. S. Losilla, P. Greco, M. Cavallini, F. Borgatti, M. Montecchi, L. Pasquali, R. Garcia, and F. Biscarini, Parallel-local anodic oxidation of silicon surfaces by soft stamps, *Nanotechnology*, **19**, 434303 (2008).
94. S. Hoeppener, R. Maoz, and J. Sagiv, Constructive microlithography: electrochemical printing of monolayer template patterns extends constructive nanolithography to the micrometer-millimeter dimension range, *Nano Lett.*, **3**, 761–767 (2003).
95. A. Zeira, D. Chowdhury, R. Maoz, and J. Sagiv, Contact electrochemical replication of hydrophilic-hydrophobic monolayer patterns, *ACS Nano*, **2**, 2554–2568 (2008).